HP1γ sets the biological age of the intestinal epithelium

Jorge Mata-Garrido[1], Yunhua Chang-Marchand[1], Claire Cherbuy[2], Eric Batsché[3], Christian Muchardt[3] and Laurence Arbibe[1*]

[1]Department of Immunology, Infectiology and Hematology, Institut Necker-Enfants Malades (INEM),INSERM U1151, CNRS UMR 8253, Université Paris Descartes, Paris, France.

[2]Commensal and Probiotics-Host Interactions Laboratory, Institut National de la Recherche Agronomique (INRA)

[3] Institut de Biologie Paris-Seine, CNRS UMR8256, Paris, France.

*Corresponding author: laurence.arbibe@inserm.fr

ABSTRACT:
Altered RNA maturation and decay have well-documented effects on tissue longevity. Yet, RNA metabolism is poorly investigated in the gut epithelium, a constantly renewing tissue particularly challenged by ageing. We found that inactivation of the epigenetic regulator HP1γ in the mouse gut epithelium results in accelerated ageing associated with both ectopic expression of ribosomal RNAs and accumulation of miss-spliced messenger RNAs. A consequence of the latter is the production of progerin, a spliced product of the *LMNA* gene associated with the Hutchinson Gilford Syndrome. Production of progerin transcript increased naturally in the mouse ageing gut, in correlation with a reduced HP1γ expression. Thus, progerin is a candidate marker of aging of the gut epithelium, while HP1γ inactivation emerges as a new model for accelerated aging in this tissue.

INTRODUCTION:

Chromatin readers encompass a variety of chromatin and transcription regulators that contain specialized domains allowing them to recognize specific histone modifications. Readers dock at specific sites and can act as adaptors to recruit molecular machineries involved in various biological events such alternative splicing, DNA repair, or recombination [1-3]. Importantly, readers initiate specific transcriptional programs playing important roles during cellular differentiation, development and in tumorigenesis, making them attractive targets for drug design [4]. Yet the analysis of their contribution to intestinal physiology remains poorly explored. Principally, the reader UHRF1 promotes colonic regulatory T cells expansion in response to the gut microbiota and the Polycomb Repressive complex 2 (PRC2) required for silencing bivalent H3K4me3- and H3K27me3-marked genes such as the cell cycle inhibitor cdkn2a, thereby restricting intestinal progenitor proliferation in response to radiation in mouse gut tissues[5,6].

The Heterochromatin Protein 1 proteins (HP1α, HP1β, and HP1γ in mouse and human) are a family of H3K9me2/3 chromatin readers. Each HP1 isoform contains two structured domains known as the chromodomain (CD) and the chromoshadow domain (CSD), separated by a flexible hinge. The CD associates with H3K9me2 and H3K9me3, while the CSD acts as a hub able to interact with a variety of chromosomal proteins regulating gene transcription [7]. The hinge domain shows RNA binding properties with non-coding pericentromeric transcript thereby seeding HP1 location at pericentromeric domain [8,9]. HP1-chromatin association is required for stable epigenetic silencing in heterochromatin, as reported in position effect variegation (PEV) studies in *Drosophila* [10]. In fission yeast, HP1 exert silencing properties through diverse mechanisms, including the association of the RNAi silencing machinery with heterochromatic transcripts, the recruitment of the SHREC histone deacetylase complex, and the degradation of heterochromatic RNA transcripts by the RNA exosome [11,12]. Moreover, structural studies suggest that HP1 is part of the mechanisms promoting phase–separated condensates that compartmentalize heterochromatin within the nucleus[13-15]. Thus, HP1 proteins are key factors in heterochromatin formation that coordinate chromatin compaction and transcriptional gene silencing. Likewise, HP1 heterochromatic functions are important for genomic stability. Indeed, HP1 loss of function in *Drosophila* and yeast system*s* leads to chromosomal compaction defects with increased DNA damage and de-repression at repeated DNA sequences, and of the rDNA locus, in particular [16-19]. Importantly, HP1 was shown to prevent unnecessary rRNA synthesis, both recognized as drivers of cell senescence and aging, and HP1 overexpression was shown to prevent heterochromatin decline frequently reported in aging [16,19]. Thus, HP1 heterochromatic functions may promote longevity, albeit its impact on mammalian aging remains elusive.

HP1 proteins also localize to actively transcribed genes in flies and mammals [20,21] . As a matter of fact, the HP1γ isoform (encoded by the gene *Cbx3*) concentrates in the coding region of active genes and interacts with the elongating RNA polymerase II (RNAPII) and the pre-mRNA[21-23]. At these intragenic positions, HP1γ may slow down transcription, possibly by decreasing RNA polymerase II elongation rate, [24] [1,25]**.** Importantly**,** genome wide *in vitro* analyses in mammalian cells also implicate HP1 in both alternative splicing (AS) and co-transcriptional RNA processing, presumably by bridging the pre-messenger RNA into chromatin and/or favoring the recruitment of the splicing machinery at methylated DNA exons [1,26-28]. Importantly, the effect of HP1γ on splicing decision has been recently linked to its

unique ability to bind intronic repetitive motif of pre-messenger RNA (). Thus, beside its function of "gate keeper " in heterochromatin stability, HP1 is expected to shape the cellular transcriptome, with central function in RNA metabolism that remains poorly explored *in vivo*.

In this work, we have interrogated the role of HP1γ in the regulation of the cellular transcriptome of the mouse intestinal epithelium and provided the seminal identification for a role of HP1γ in the homeostatic control of RNA metabolism in relation with tissue longevity.

RESULTS AND DISCUSSION:

HP1γ null mutations are embryonic lethal at a high rate [29]. We therefore generated a Villin-creERT2:*Cbx3-/-* mouse model, allowing inactivation of HP1γ in the epithelial lineage of the gut upon tamoxifen administration. As reported for other models of *Cbx3* knockout (KO), we noted a time-dependent compensatory up-regulation of other HP1 isoforms in both crypt and villi (**Supplementary figure 1A**)[30]. To investigate the impact of HP1γ inactivation on heterochomatin stability, we looked at accumulation of the constitutive heterochromatic markers histone H3 trimethyl Lys9 (H3K9me3) and histone H4 trimethyl Lys20 (H4K20me3). Reminiscent of the phenotype obtained upon *Cbx3* inactivation in adult cardiac myocytes, H4K20me3 levels -but not those of H3K9me3- were severely impaired in the gut epithelium (**Supplementary figure 1B-C)** [30]. The H4K20me3 histone mark is important for the silencing of repetitive DNA, including ribosomal DNA repeats. We thus investigated the impact of *Cbx3* on the stability of nucleoli. A gradual decline in nucleoli organelles along the villi has been reported, suggesting that post-mitotic cell populations of the gut epithelium normally thrive on ribosomes inherited from the progenitor cells [31]. Likewise, expression of nucleolin, a marker of the nucleolus, declines along the crypt-villus axis (**Figure 1A**). By contrast, in *Cbx3* KO mice, there was a persistent nucleolin staining along the villi, and electron microcopy studies provided further evidence for the presence of nucleoli at the upper part of the villi, with detectable granular components and fibrillar centers, the latter containing rRNAs **(Figures 1A and 1D)**. Finally, RT-qPCR analysis showed increased rRNA accumulation, especially at the villi compartment, while genome-wide RNA-seq on purified epithelial cells showed enrichment in genes involved in ribosomal biogenesis (**Figure 1B-C**). Overall, these data showed that *Cbx3* keeps rDNA transcription in check and is responsible for the homeostatic repression of nucleolar organelle naturally occurring during epithelial cell maturation. Dysregulation of rRNA synthesis is a driver of aging in various models, possibly through metabolic exhaustion limiting cell renewal, and nucleolar expansion has been reported in primary fibroblast from Hutchinson Gilford Syndrome (HGPS) patients [32]. Moreover, HGPS fibroblast showed evidence for deficient HP1 expression [33]. We thus search whether young *Cbx3* KO mice displayed sign of accelerated aging. Depending on the models, aging in intestinal stem cell (ISC) has been associated with increase in ISC proliferation, but with functional declines illustrated by ISC maturation defects leading to the accumulation of miss-differentiated daughter cells retaining stemness marks and a poor regenerative potential presumably linked to a deficiency in Wnt signaling [34 35 36]. *Cbx3* inactivation in 2-3 months-old mice led to an expansion of KI67+ along the crypt-villi axis (**Figure 2A**). Moreover, while BrdU incorporation was primarily seen in the TA cells in vehicle-treated mice, it was strongly detected in cells at the base of the crypts in *Cbx3* KO mice, providing evidence for enhanced proliferation in the stem cell compartment (**Figure 2B**). Likewise, in organoids derived from *Cbx3* KO mice, we noted an

aberrant detection of EdU positive cells (marker of S phase of the cell cycle) along the villi domain axis also accumulating into the lumen of the organoids (**Figure 2C**) Finally, reminiscent of the aged *Drosophila* midgut model, the monolayer organization of the epithelium of the intestinal crypts was altered, with proliferative cells clustering in the gut lumen (**Figure 2B6**). Overall these data suggested that HP1γ prevented a deregulated proliferative state in the intestinal crypts. We next evaluated the impact of HP1γ on ISC functional activities. As a validated *ex vivo* assay reflecting stem cell function *in vivo*, we first analyzed the rate of bud formation per crypt in organoid cultures. Bud formations after the second passage were severely affected in the organoids derived from *Cbx3* KO mice, revealing a decline in the regenerative potential, possibly as a consequence of cellular exhaustion or maturity defects impairing crypt formation (**Figure 2D**). To further investigate the impact of HP1γ on lineage maturation, we isolated epithelial cells from crypts and villi, and performed RNA-seq. Maturation defects in aging have been reported in the *Drosophila* midgut, at best illustrated by the retention of stemness mark in progeny [34]. We thus looked at typical ISC-specific markers, namely the Notch-target gene Olfm4 and the Wnt-target genes lgr5 or Ascl2. While Q-PCR data didn't show significant transcriptional changes, *Cbx3* inactivation at the intestinal crypt principally affected Olfm4 expression, as shown by an extended zone of detection of the Olfm4 signal along the crypt (**Figure 2E1-E5**). In the villi, RNA seq and Q-PCR data provided evidence for the transcriptional persistence of stemness marks, including Ascl2 and Olfm4, highlighting unresolved differentiation process (**Figure 2E6)**.Consequently, the production of mature lineages in the *Cbx3* mice were globally affected on both absorptive and secretory lineages. In particular, gsea analysis showed alterations in the Paneth and enterocyte genes expression programs **(Figure 2F)**, further confirmed by a marked loss of lysozyme detection by IF (Paneth cell marker) or Sucrase Isomaltase expression protein level (enterocyte differentiation) (**Figure 2G-H)**. Due to their ability to secrete anti-microbial peptides, Paneth cell are essential for the maintenance of the microbiota, preventing deleterious shifts in the bacterial community [37]. We thus explored the impact of HP1γ deficiency on host fecal microbiota by 16S rRNA gene sequencing. The fecal microbiota of the *Cbx3* mice was highly dysbiotic, with a bloom of *Enterobacteriaceae* and *Bacteroidaceae* including the *Alistipes* genus which in both mouse and human microbiota studies, is strongly associated with the gut microbiome in the elderly (**Supplementary figure 2)** [38] [39]. Overall, these data showed that loss of HP1γ in young mice speeds up the appearance of functional deficiencies featured by the aging gut across the species. In particular, the homeostatic control exerted by *Cbx3* on progenitor proliferation and on nucleolar activity might contribute to preserve tissue longevity by preventing tissue exhaustion. However, as a regulator of splicing decisions, HP1γ might also contribute to longevity *via* RNA metabolic functions. Interestingly, the aging phenotype in HGPS patients is causally linked to increased usage of an alternative 5' splice site (SS) in exon 11 of the *LMNA* pre-mRNA, thereby producing a truncated splice-variant encoding progerin. We thus questioned whether HP1γ inactivation would trigger the production of spliced variants causally linked to aging, with a particular interest for those encoding progerin. We first analyzed the global impact of HP1γ on splicing in the RNA-seq data using rMATS(replicate Multivariate Analysis of Transcript Splicing) algorithm. HP1γ inactivation had an extensive effect on the outcome of splicing both in crypt and villus epithelia, changing the ratio between numerous splicing variants, frequently as a consequence of intron retention (**Table 1**). To investigate the possible involvement of HP1γ in the regulation of *LMNA* gene spliced variants, we used a

taqman assay distinguishing between lamin A and progerin. After validation by end-point RT-qPCR and sequencing, the assay showed that lamin A transcripts were up-regulated upon *Cbx3* inactivation in both crypts and villi (**Figure 3A**). The sequencing of the PCR products further confirmed the production of progerin transcripts in these cells (**Figure 3B**). Moreover, in the *Cbx3* KO mice, progerin protein production was evidenced in both crypts and villi by immunoblot (**Figure 3C**). Finally, IF analysis detected nuclear progerin in both villi and crypts. In the latter tissue, progerin was principally detected at in the immediate progeny of the stem cells (**Figure 3D**). Overall, these data showed that HP1γ repressed the production of lamin A spliced variants, including progerin in the gut epithelium. We next explored whether high progerin- and low HP1γ-levels could be used as markers during normal aging of the gut epithelium. When comparing mice aged 4-months and 19-months (onset of aging), HP1γ expression was reduced in the crypt epithelium of the aged mice, while remaining essentially unmodified in the villi, as shown by IF and immunoblot analysis (**Figure 4A-B).** For lamin A, transcript levels showed a moderate but significant increase in both crypts and villi upon aging, while expression of progerin transcripts was strongly up-regulated (**Figure 4C).** At the protein level, progerin showed an increase, only detectable at the aged crypt epithelium, suggesting homeostatic mechanisms aimed at preventing protein production and/or favoring its degradation in villi compartment (**Figure 4D).** Overall, these data provide evidence that aging alters HP1γ expression in the gut epithelium and identified the lamin A spliced variant progerin as a new marker of the aging gut epithelium.

In conclusion, this study propels HP1 as a major regulator of RNA metabolism in the gut epithelium. Active both at protein-coding genes and on rDNA, HP1 is ideally suited for recruiting machineries silencing rRNA or promoting RNA splicing thereby exerting functions in RNA homeostasis with relevance for aging. The gut epithelium is a constantly renewing tissue thereby particularly challenged by aging**.** Elucidating the mechanisms altering HP1 splicing activities over life-time should provide new strategies for preserving tissue longevity.

MATERIEL AND METHODS

Mouse models

Cbx3$^{fl/fl}$ mice were provided by Dr Florence Cammas and crossed with Villin-CreERT2 mice to produce the Villin-creERT2:*Cbx3-/-* mice model (this study). Mice were fed a standard diet (SD) rodent chow (2018 Teklad Global 18% Protein Rodent Diet, Harlan) composed of 60% carbohydrate fed *ad libitum*. Tamoxifen administration by gavage 20% clinoleic acid was performed as described, with 3 dosis, one every 5 days [40]. Control mice received 20% clinoleic acid alone by gavage. Additional controls using *Cbx3*$^{fl/fl}$ mice that do not express the Cre recombinase were identically treated with tamoxifen. With the exception of the experiments with aged mice, all the experiments were performed with 2-3 months aged mice.

Tissue processing for histology

Mice were sacrified by cervical dislocation. Intestine (ileum or colon) was collected and washed with PBS at 4ºC and cut in pieces about 5 mm. Intestinal fragments were fixed with formalin overnight at 4ºC. Once fixed, intestinal fragments were

included in paraffine blocks. Paraffine sections were done in a microtome Leica RM2125 RTS, with a thickness of 4μm. Subsequently, the deparaffinization and rehydration of the samples was carried out by immersion in Xylene (2x10 min), absolute ethanol 5 min, 90% ethanol 5 min, 70% ethanol 5 min and distilled water (2x5 min), all at R.T. Finally, the antigen was unmasked using the EDTA boiling technique for 30 min at 95ºC, followed by 20 min at R.T. All samples were sequentially treated with 0.1 M glycine in PBS for 15 min, 3% BSA in PBS for 30 min and 0.5% Triton X-100 in PBS for 2h (mouse tissue). They were then incubated with primary antibodies overnight at 4 °C, washed with 0.05% Tween-20 in PBS, incubated for 1h in the specific secondary antibody conjugated with Alexa 488 or Cy3 (Jackson, USA), 15 min with DAPI (1μg/ml), washed in PBS and mounted with the antifading medium VECTASHIELD® (Vector laboratories). Microscopy images were obtained with a ZEISS Apotome.2 (Zeiss, Germany), structured illumination microscope, using a 63× oil (1.4 NA) objective. To avoid overlapping signals, images were obtained by sequential excitation at 488 and 543 nm in order to detect A488 and Cy3, respectively. Images were processed using ZEISS ZEN lite software. The quantitative analysis of the immunofluorescence umages and their posterior image processing and measurement steps were performed on ImageJ, public domain software for image analysis (NIH, Bethesda, Maryland, USA; http://rsb.info.nih.gov/ij/). Data were analyzed using GraphPad software and one-way ANOVA was used to determine the statistical significance of differences between control and the different experimental condictions. Values are represented with Mean +/- SD.

Transmission electron microscopy

Transmission electron microscopy was realized as previously described [41]. Conventional ultrastructural examination of Caco‑2/TC7 cells, C57BL/6 WT and CBX3 KO (n = 3 per group) were fixed with 1% paraformaldehyde and 1% glutaraldehyde in 0.1 M phosphate buffer, pH 7.4. DRG were removed, rinsed in 0.1 M phosphate buffer, postfixed in 2% osmium tetroxide, dehydrated in acetone and embedded in araldite (Durcupan, Fluka, Switzerland). Ultrathin sections stained with uranyl acetate and lead citrate were examined with a JEOL 201 electron microscope.

Tissue processing for intestinal epithelial cells isolation and organoids culture

The technique was adapted from Nigro et al, 2019 [42]. Mice were sacrified by cervical dislocation. Small intestine was collected and washed with PBS at 4ºC and cut in pieces about 5 mm. Intestinal fragments were incubated 30 min at 4ºC in 10mM EDTA after which intestinal fragments were tranfer to BSA 0,1% in PBS and vortexed between 30 s and 1 min. Supernatant was filtered with a 70μm cell strainer. At this step, crypts went through the cell strainer and villi were retained on it. To isolate epithelial cells, crypts and villi fractions were centrifuged separately and the pellet was frozen in liquid nitrogen until processed. For organoid production, crypt pellet was disgregated and cultured in Matrigel as described [42].

Real time quantitative PCR (RTqPCR) for relative gene expression analysis

Total RNA was extracted and cleaned from Caco‐2/TC7 cells or intestinal epitelial cells purified from mice (n = 3 minimum per group) using Trizol (TR-118, Molecular Research Center, Inc.) following the manufacturer's instructions. Three animals per group were used. RNA samples were quantified using a spectrophotometer (Nanodrop Technologies ND-1000). First-strand cDNA was synthesized by RT-PCR using a RevertAIT H Minus First Strand cDNA Synthesis kit (Thermo Scientific). The cDNA concentration was measured in a spectrophotometer (Nanodrop Technologies ND-1000) and adjusted to 0.3 mg/ml. qPCR was performed using the Mx3005P system (Stratagene) with automation attachment. In this work, we have used SYBRGreen (Takara) based qPCR. *GAPDH* was chosen as the normalizer in our experiments. Expression level was evaluated relative to a calibrator according to the 2-(DDCt) equation. Mean values for fold changes were calculated for each gene. The relative levels of 45S pre-rRNA and mature 18S rRNA were calculated as previously reported [43]. Each value in this work represents the mean ± SD of at least 3 independent samples obtained under the same conditions. Data were analyzed using one-way ANOVA followed by Bonferroni tests for comparisons. Statistical significance was set at $p < 0.05$. For progerin and laminA detection, real-time PCR amplification was carried out with the TaqMan" Gene Expression Master Mix (life technologies) using predesigned primers for mouse GAPDH (Mm99999915_g1), mouse lamin A primers that do not recognized progerin or DNA (Assay ID : APGZJEM), mouse progerin primers (F: ACTGCAGCGGCTCGGGG. R: GTTCTGGGAGCTCTGGGCT and probe: CGCTGAGTACAACCT).

Total RNA preparation and sequencing for transcriptome analysis

Total RNA was prepared out from control and *Cbx3* KO purified crypt and villi epithelium (3 mice for each group) by guanidinium thiocyanate-phenol- chloroform extraction according to the method of Chomczynski and Sacchi[44], followed by proteinase K and DNAse treatments as described above. Total RNA library preparation and sequencing were performed on DNase-treated RNA samples by Novogene Co., Ltd, as a lncRNA sequencing service, including lncRNA directional library preparation with rRNA depletion (Ribo-Zero Magnetic Kit), quantitation, pooling and PE 150 sequencing (30G raw data-100M raw reads/sample) on Illumina HiSeq 2500 platform. For Alternative Splicing Analysis, rMATS(replicate Multivariate Analysis of Transcript Splicing) has been used for detection of differential alternative splicing events from RNA-Seq data. rMATS uses a hierarchical model to simultaneously account for sampling uncertainty in individual replicates and variability among replicates. Classification and statistics of AS events are applied to each group of RNA-seq data with biological replicates. Then the quantitative level of each class of alternative splicing events is estimated, and differential AS analysis between treatment and control groups are applied. rMATS adopts two quantification methods parallel, namely evaluating splicing with reads span splicing junctions only, and with both reads on target and reads span splicing junctions. The expression level of different AS types for individual genes in both treatment and control groups of

samples is analyzed and the threshold of differential AS analysis is set as FDR < 0.05.

Fecal microbiota analysis by 16S rRNA gene sequencing

Genomic DNA was obtained from faecal or caecal samples using the QIAamp power fecal DNA kit (Zymo Research), and DNA quantity was determined using a TECAN Fluorometer (Qubit® dsDNA HS Assay Kit, Molecular Probes). The V3-V4 hypervariable region of the 16S rRNA gene was amplified by PCR using the following primers: a forward 43-nuclotide fusion primer 5′ **CTT TCC CTA CAC GAC GCT CTT CCG ATC T**AC GGR AGG CAG CAG3′ consisting of the 28-nt illumina adapter (bold font) and the 14-nt broad range bacterial primer 343F and a reverse 47-nuclotide fusion 5′ **GGA GTT CAG ACG TGT GCT CTT CCG ATC T**TA CCA GGG TAT CTA ATC CT3′ consisting of the 28-nt illumina adapter (bold font) and the 19-nt broad range bacterial primer 784R. The PCR reactions were performed using 10 ng of DNA, 0.5 µM primers, 0.2 mM dNTP, and 0.5 U of the DNA-free Taq-polymerase, MolTaq 16S DNA Polymerase (Molzym). The amplifications were carried out using the following profile: 1 cycle at 94° C for 60 s, followed by 30 cycles at 94° C for 60 s, 65° C for 60 s, 72° C for 60 s, and finishing with a step at 72° C for 10 min.The PCR reactions were sent to the @Bridge platform (INRAe, Jouy-en-Josas) for sequencing using Illumina Miseq technology. Single multiplexing was performed using home-made 6 bp index, which were added to R784 during a second PCR with 12 cycles using forward primer (AATGATACGGCGACCACCGAGATCTACACTCTTTCCCTACACGAC) and reverse primer(CAAGCAGAAGACGGCATACGAGAT-index GTGACTGGAGTTCAGACGTGT).The resulting PCR products were purified and loaded onto the Illumina MiSeq cartridge according to the manufacturer instructions. The quality of the run was checked internally using PhiX, and then, sequences were assigned to its sample with the help of the previously integrated index. High quality filtered reads were further assembled and processed using FROGS pipeline (Find Rapidly OTU with Galaxy Solution) to obtain OTUs and their respective taxonomic assignment thanks to Galaxy instance [45] (https://migale.inra.fr/galaxy) In each dataset, more than 97% of the paired-end sequences were assembled using at least a 10-bp overlap between the forward and reverse sequences. The following successive steps involved de-noising and clustering of the sequences into OTUs using SWARM, chimera removal using VSEARCh. Then, cluster abundances were filtered at 0.005%. One hundred percent of clusters were affiliated to OTU by using a silva138 16S reference database and the RDP (Ribosomal Database Project) classifier taxonomic assignment procedure. Richness and diversity indexes of bacterial community, as well as clustering and ordinations, were computed using the Phyloseq package (v 1.19.1) in RStudio software [46].Divergence in community composition between samples was quantitatively assessed by calculating β-diversity index (UniFrac and weighted UniFrac distance matrices). Within sample community

α-diversity was assessed by observed diversity (i.e. sum of unique OTUs per sample) and Shannon index, eveness-based richness indices.
Unconstrained ordination was visualised using multidimensional scaling (MDS) and hierarchical clustering (complete linkage combined with wUniFrac distance) and compared using Adonis test (9999 permutations).

SDS-PAGE and immunoblotting
Intestinal epithelial cells purified from mice (n = 3 minimum per group) were lysed at 4 °C in a buffer containing 25mM Tris pH 7.5, 1mM EDTA, 0.1mM EGTA, 5mM $MgCl_2$, 1% NP-40, 10% Glycerol, 150mM NaCl, and then cleared by centrifugation at 14,000 rpm for 30 min at 4 °C. Proteins were separated on SDS–PAGE gels and transferred to nitrocellulose membranes by standard procedures. Mouse anti-progerin monoclonal antibody (sc-81611, Santa Cruz Biotechnology, Inc) was used at 1:500 dilution for the Western blot analyses and for immunofluorescence labeling.

Statistical Analyses
p values were calculated using Prism (GraphPad). Differences between the two groups were tested with a Student's t test, and the differences between three or more groups were tested by one-way ANOVA.

ACKNOWLEDGMENTS
We thank Florence Cammas for providing the *Cbx3*$^{fl/fl}$ mice.

FUNDINGS
This work has been supported by the «Agence National de la Recherche» (ANR) grant
(EPI-CURE, R16154KK)

FIGURE LEGENDS
Figure 1. HP1γ represses nucleor activities in the villi (A) In physiological condition, the nucleolus is mainly detected at the intestinal crypt (A1-A6), while *Cbx3* inactivation leads to the detection of this organelle throughout the entire intestinal villi (A4 -A6) Scale bar: 80µm. (B) rRNA expression levels detected by RT-qPCR. The immature 45S form is not altered, in both crypt and villi (B1), while the mature 18S form accumulates in both crypt and villi in the *Cbx3* KO mice(B2). The statistical analysis was carried out in three different animals, using a *t test* at a 95% confidence interval. (C) Gsea analysis of the enrichment in mRNAs associated with ribosome biogenesis in *Cbx3* KO vs Control, obtained by RNA-seq, specifically in villi (n = 3). (D) Characterization of the nucleolar structure in differentiated cells of the upper part of the villi by transmission electron microscopy (TEM). The presence of heterochromatin can be observed in the nucleus of control mice (D1-D2), but no nucleolus was observed. In contrast, the same cells from *Cbx3* KO mice present canonical nucleoli (D3-D4) Scale bar: D1, D3=5µm; D2, D4= 1µm.

Suplementary figure 1. Validation of the *Cbx3* KO model *in vivo*. (A) HP1γ expression in lost after tamoxifen administration by oral gavage. This event leads to a time dependant increase in proteins HP1α and HP1β, probably as a compensatory mechanism. This process takes place both in the crypt (A1) and in the villi (A2). (B) IF showing a loss of HP1γ detection while H3K9m3 is not affected. HP1γ is present in the nucleous of epithelial cells in vehicle treated (ctrl) mice (B1-B4) and expression lost upon. tamoxifen administration (B5-B8). *Cbx3* KO is epithelial-specific as HP1γ is detected in the nuclei of the lamina propria cells (B7). (C) *Cbx3* KO leads to a decrease of the histone mark H4K20m3 in epitelial cells Scale bar: 80µm.

Figure 2. HP1γ regulates the proliferation and maturation of the gut epithelium (A) IF showing Ki67 cells principally detected in TA cells in control mice (A1-A3), while in *Cbx3* KO, Ki67 cells could be detected at the bottom of the crypt and initial part of the villi (A4-A6). Scale bar: 80µm. (B) BrdU positive cells are detected in the transit amplifying cells 2h in control mice (B1-B3), while it can be detected also at the bottom of the crypt in the *Cbx3* KO mice (B4-B6, insert). Inside the crypt, cells with loss of polarity forming clusters could be detected (white arrows). Scale bar: B1-B6=50µm; Insert=15µm. (C) EdU staining is found on the crypts in control organoids (C1-C3), and never in the villi. In *Cbx3* KO organoids, Edu can be detected in the villi (C4-C6), in approximatively 24% of the cells (C7). Counting was carried out using Fiji software. The statistical analysis was carried out in 3 different animals, using a *t test* at a 95% confidence interval. Scale bar: 100µm. (D) After 10 days of differentiation, the control organoids are completely differentiated, presenting a multitude of invaginations, where the crypts are found (D1). However, the *Cbx3* KO organoids exibit a significantly lower number of invaginations, as well as a larger size (D2-D3). Counting was carried out using Photoshop counting tool. The statistical analysis was carried out in three different animals, using a *t test* at a 95% confidence interval. (E) The stem cell marker Olfm4 is located at the bottom of the crypt in control animals (E1), occupying a very well defined area, while in *Cbx3* KO a significant increase in this area (E2-E4) can be seen, as well as a progression towards the villi (E2-E3). Scale bar: 40µm. The statistical analysis was carried out in six different animals, measuring a minimum of 20 fields per animal, by one-way ANOVA. RT-qPCR analysis of gene expression asociated with stem cells shows an significative increase specifically in the villi (E6), but no differences where found in the crypt (E5). The statistical analysis was carried out in three different animals, using a *t test* at a 95% confidence Interval. ((F)F Gene set enrichment analyses (Gsea) representing an inverse correlation between *Cbx3* KO and control for ISC signature, and enterocyte at the villi and Paneth cells in the crypt. The ISC signature is not affected at the intestinal crypt. (G) Western blot analysis of sucrase-isomaltase (Sis), a marker of enterocytic differentiation (H) IF showing lysozyme expression , a marker of Paneth cells . The statistical analysis was carried out in six different animals, measuring a minimum of 20 fields per animal, by one-way ANOVA.

Figure 3. HP1γ regulates alternative splicing of the *LMNA* gene. In each experiment, HGPS MEF were used as internal control (A) RT-qPCR analysis of LaminA expression in both crypt and villi (A1). The statistical analysis was carried out in four different animals, by one-way ANOVA. The analysis of the RT-qPCR end products on 2% agarose gel showing an unique band at the predicted molecular weight (A2). RT-qPCR analysis of progerin expression (B1). The statistical analysis was carried out in four different animals, by one-way ANOVA. The analysis of the RT-qPCR end products on 2% gel shows the LaminA band, still detectable, in the control, whereas after tamoxifen treatment, a lower molecular weight band corresponding to the predicted molecular weight for progerin appeared in both crypt and villi in *Cbx3* KO mice (B2). (B3) showed an example of the sequencing data obtained after gel excision of the predicted progerin band (C) Protein analysis by western blot of progerin levels. Loss of HP1γ allows detection of progerin, while it is undetectable in both control or Cbx3 fl/fl treated with tamoxifen. (D) Progerin is undetectable by immunofluorescence in control, in both crypt (D4-D6) and villi (D1-D3), while in *Cbx3* KO an intense and specific marking is seen in the nucleus of epithelial cells in both crypt (D10-D12) an villi (D7-D9). Note that the stem cell compartment (bottome of the crypt) is devoid of progerin staining (D10-D12, separated by point lines). Scale bar: 100μm

Figure 4. Progerin marks the aging gut in correlation with HP1g deficiency (A) IF study showing that HP1γ is found in the nucleus of epithelial cells in young adult mice (4 months) at both crypt and villi, although with less intensity in the latter compartment (A1-A6). In aged mice (19 months), HP1γ is poorly detected at the intestinal crypt, in particular at the stem cell compartment (A10-A12, separated by dotted line) Scale bar: 100 μm. (B) Western blot analysis showing a decrease in HP1γ protein levels in aged mice (19 months), as compared to Young adult mice (4 months) specifically in the crypt compartment. (C) RT-qPCR analysis reveals a significative increase in both laminA mRNA (C1) and progerin (C2) in old mice, 19 months, compared to young mice, 4 months, in both crypt and villi. The statistical analysis was carried out in three different animals, using a *t test* at a 95% confidence interval. The analysis of the RT-qPCR end products on 2% agarose gel shows the laminA band, still detectable, in the Young 4 months old mice, whereas in the aged 19 months old mice, only a lower molecular weight band can be detected, at the expected size of progerin, in both crypt and villi (C3). (D) Western blot analysis reveals an increase in progerin protein levels in old mice, 19 months, compared to young mice, 4 months, specifically in the crypt compartment.

Table1.

Total number of differential AS events Tamox versus vehicle, (up: down)

SE: Skipped exon
MXE: Mutually exclusive exons
A5SS: Alternative 5' splice site

A3SS: Alternative 3' splice site
RI: Retained intron

NumEvents.JC.only: the total number of AS events, with only the reads span splicing junctions taken into account. (up:down).

SigEvents.JC.only: the total number of differential AS events, with only the reads span splicing junctions taken into account

BIBLIOGRAPHY

1. Saint-André, V., Batsche, E., Rachez, C. & Muchardt, C. Histone H3 lysine 9 trimethylation and HP1γ favor inclusion of alternative exons. *Nat. Struct. Mol. Biol.* **18,** 337–344 (2011).
2. Chen, J. *et al.* TRIM66 reads unmodified H3R2K4 and H3K56ac to respond to DNA damage in embryonic stem cells. *Nat Commun* **10,** 4273–17 (2019).
3. Mandal, M. *et al.* Histone reader BRWD1 targets and restricts recombination to the Igk locus. *Nat. Immunol.* **16,** 1094–1103 (2015).
4. Mio, C., Bulotta, S., Russo, D. & Damante, G. Reading Cancer: Chromatin Readers as Druggable Targets for Cancer Treatment. *Cancers (Basel)* **11,** 61 (2019).
5. Chiacchiera, F., Rossi, A., Jammula, S., Zanotti, M. & Pasini, D. PRC2 preserves intestinal progenitors and restricts secretory lineage commitment. *EMBO J.* **35,** 2301–2314 (2016).
6. Jadhav, U. *et al.* Acquired Tissue-Specific Promoter Bivalency Is a Basis for PRC2 Necessity in Adult Cells. *Cell* **165,** 1389–1400 (2016).
7. Eissenberg, J. C. & Elgin, S. C. R. HP1a: a structural chromosomal protein regulating transcription. *Trends Genet.* **30,** 103–110 (2014).
8. Muchardt, C. *et al.* Coordinated methyl and RNA binding is required for heterochromatin localization of mammalian HP1alpha. *EMBO Rep.* **3,** 975–981 (2002).
9. Maison, C. *et al.* SUMOylation promotes de novo targeting of HP1α to pericentric heterochromatin. *Nat. Genet.* **43,** 220–227 (2011).
10. Eissenberg, J. C. *et al.* Mutation in a heterochromatin-specific chromosomal protein is associated with suppression of position-effect variegation in Drosophila melanogaster. *Proc. Natl. Acad. Sci. U.S.A.* **87,** 9923–9927 (1990).
11. Motamedi, M. R. *et al.* HP1 proteins form distinct complexes and mediate heterochromatic gene silencing by nonoverlapping mechanisms. *Mol. Cell* **32,** 778–790 (2008).
12. Keller, C. *et al.* HP1(Swi6) mediates the recognition and destruction of heterochromatic RNA transcripts. *Mol. Cell* **47,** 215–227 (2012).
13. Strom, A. R. *et al.* Phase separation drives heterochromatin domain formation. *Nature* **547,** 241–245 (2017).
14. Larson, A. G. *et al.* Liquid droplet formation by HP1α suggests a role for phase separation in heterochromatin. *Nature* **547,** 236–240 (2017).
15. Sanulli, S. *et al.* HP1 reshapes nucleosome core to promote phase separation of heterochromatin. *Nature* **575,** 390–394 (2019).
16. Sinclair, D. A. & Guarente, L. Extrachromosomal rDNA circles--a cause of aging in yeast. *Cell* **91,** 1033–1042 (1997).

17. Peng, J. C. & Karpen, G. H. H3K9 methylation and RNA interference regulate nucleolar organization and repeated DNA stability. *Nat. Cell Biol.* **9,** 25–35 (2007).
18. Yan, S.-J., Lim, S. J., Shi, S., Dutta, P. & Li, W. X. Unphosphorylated STAT and heterochromatin protect genome stability. *FASEB J.* **25,** 232–241 (2011).
19. Larson, K. *et al.* Heterochromatin formation promotes longevity and represses ribosomal RNA synthesis. *PLoS Genet.* **8,** e1002473 (2012).
20. Piacentini, L., Fanti, L., Berloco, M., Perrini, B. & Pimpinelli, S. Heterochromatin protein 1 (HP1) is associated with induced gene expression in Drosophila euchromatin. *J. Cell Biol.* **161,** 707–714 (2003).
21. Vakoc, C. R., Mandat, S. A., Olenchock, B. A. & Blobel, G. A. Histone H3 lysine 9 methylation and HP1gamma are associated with transcription elongation through mammalian chromatin. *Mol. Cell* **19,** 381–391 (2005).
22. Mateescu, B., Bourachot, B., Rachez, C., Ogryzko, V. & Muchardt, C. Regulation of an inducible promoter by an HP1beta-HP1gamma switch. *EMBO Rep.* **9,** 267–272 (2008).
23. Lomberk, G., Bensi, D., Fernandez-Zapico, M. E. & Urrutia, R. Evidence for the existence of an HP1-mediated subcode within the histone code. *Nat. Cell Biol.* **8,** 407–415 (2006).
24. Hwang, K. K., Eissenberg, J. C. & Worman, H. J. Transcriptional repression of euchromatic genes by Drosophila heterochromatin protein 1 and histone modifiers. *Proc. Natl. Acad. Sci. U.S.A.* **98,** 11423–11427 (2001).
25. Harouz, H. *et al.* Shigella flexneri targets the HP1γ subcode through the phosphothreonine lyase OspF. *EMBO J.* **33,** 2606–2622 (2014).
26. Ameyar-Zazoua, M. *et al.* Argonaute proteins couple chromatin silencing to alternative splicing. *Nat. Struct. Mol. Biol.* **19,** 998–1004 (2012).
27. Smallwood, A. *et al.* CBX3 regulates efficient RNA processing genome-wide. *Genome Res.* **22,** 1426–1436 (2012).
28. Yearim, A. *et al.* HP1 is involved in regulating the global impact of DNA methylation on alternative splicing. *Cell Rep* **10,** 1122–1134 (2015).
29. Aydin, E. *et al.* A hypomorphic Cbx3 allele causes prenatal growth restriction and perinatal energy homeostasis defects. *J. Biosci.* **40,** 325–338 (2015).
30. Oyama, K. *et al.* Deletion of HP1γ in cardiac myocytes affects H4K20me3 levels but does not impact cardiac growth. *Epigenetics Chromatin* **11,** 18–15 (2018).
31. Altmann, G. G. A gradual decrease in nucleolar size with the maturation of columnar epithelial cells in the adult rat intestine under normal and various experimental conditions. *J. Cell. Sci.* **77,** 289–304 (1985).
32. Buchwalter, A. & Hetzer, M. W. Nucleolar expansion and elevated protein translation in premature aging. *Nat Commun* **8,** 328–13 (2017).
33. Scaffidi, P. & Misteli, T. Lamin A-dependent misregulation of adult stem cells associated with accelerated ageing. *Nat. Cell Biol.* **10,** 452–459 (2008).
34. Biteau, B., Hochmuth, C. E. & Jasper, H. JNK activity in somatic stem cells causes loss of tissue homeostasis in the aging Drosophila gut. *Cell Stem Cell* **3,** 442–455 (2008).
35. Moorefield, E. C. *et al.* Aging effects on intestinal homeostasis associated with expansion and dysfunction of intestinal epithelial stem cells. *Aging (Albany NY)* **9,** 1898–1915 (2017).
36. Nalapareddy, K. *et al.* Canonical Wnt Signaling Ameliorates Aging of Intestinal Stem Cells. *Cell Rep* **18,** 2608–2621 (2017).
37. Riba, A. *et al.* Paneth Cell Defects Induce Microbiota Dysbiosis in Mice and

Promote Visceral Hypersensitivity. *Gastroenterology* **153,** 1594–1606.e2 (2017).
38. Langille, M. G. *et al.* Microbial shifts in the aging mouse gut. *Microbiome* **2,** 50–12 (2014).
39. Claesson, M. J. *et al.* Gut microbiota composition correlates with diet and health in the elderly. *Nature* **488,** 178–184 (2012).
40. Le Gallou, S., Nojima, T., Kitamura, D., Weill, J.-C. & Reynaud, C.-A. The AID-Cre-ERT2 Model: A Tool for Monitoring B Cell Immune Responses and Generating Selective Hybridomas. *Methods Mol Biol* **1623,** 243–251 (2017).
41. Mata-Garrido, J. *et al.* Persistent accumulation of unrepaired DNA damage in rat cortical neurons: nuclear organization and ChIP-seq analysis of damaged DNA. *Acta Neuropathol Commun* **6,** 68–15 (2018).
42. Nigro, G., Hanson, M., Fevre, C., Lecuit, M. & Sansonetti, P. J. Intestinal Organoids as a Novel Tool to Study Microbes-Epithelium Interactions. *Methods Mol Biol* **1576,** 183–194 (2019).
43. Palanca, A., Casafont, I., Berciano, M. T. & Lafarga, M. Reactive nucleolar and Cajal body responses to proteasome inhibition in sensory ganglion neurons. *Biochim Biophys Acta* **1842,** 848–859 (2014).
44. Chomczynski, P. & Sacchi, N. The single-step method of RNA isolation by acid guanidinium thiocyanate-phenol-chloroform extraction: twenty-something years on. *Nat Protoc* **1,** 581–585 (2006).
45. Escudié, F. *et al.* FROGS: Find, Rapidly, OTUs with Galaxy Solution. *Bioinformatics* **34,** 1287–1294 (2018).
46. McMurdie, P. J. & Holmes, S. Phyloseq: a bioconductor package for handling and analysis of high-throughput phylogenetic sequence data. *Pac Symp Biocomput* 235–246 (2012).

Fig.1

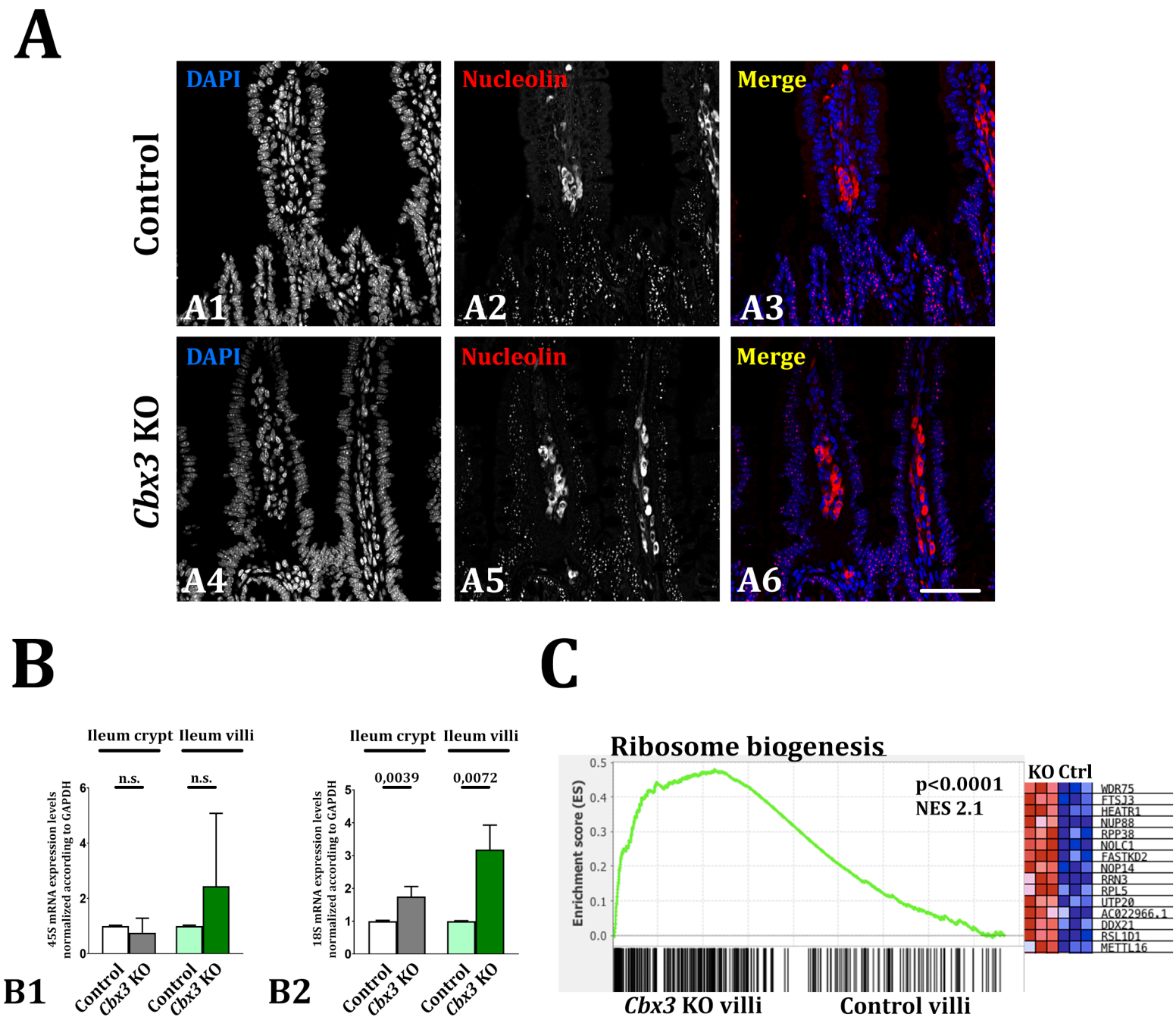
A
Control
Cbx3 KO
DAPI
Nucleolin
Merge
A1
A2
A3
A4
A5
A6
B
Ileum crypt
Ileum villi
n.s.
n.s.
45S mRNA expression levels normalized according to GAPDH
Control
Cbx3 KO
B1
0,0039
0,0072
18S mRNA expression levels normalized according to GAPDH
B2
C
Ribosome biogenesis
Enrichment score (ES)
p<0.0001
NES 2.1
KO Ctrl
WDR75
FTSJ3
HEATR1
NUP88
RPP38
NOLC1
FASTKD2
NOP14
RRN3
RPL5
UTP20
AC022966.1
DDX21
RSL1D1
METTL16
Cbx3 KO villi
Control villi
D
Control
hc
D1
D2
Cbx3 KO
n
D3
g
fc
dfc
D4

Fig.2

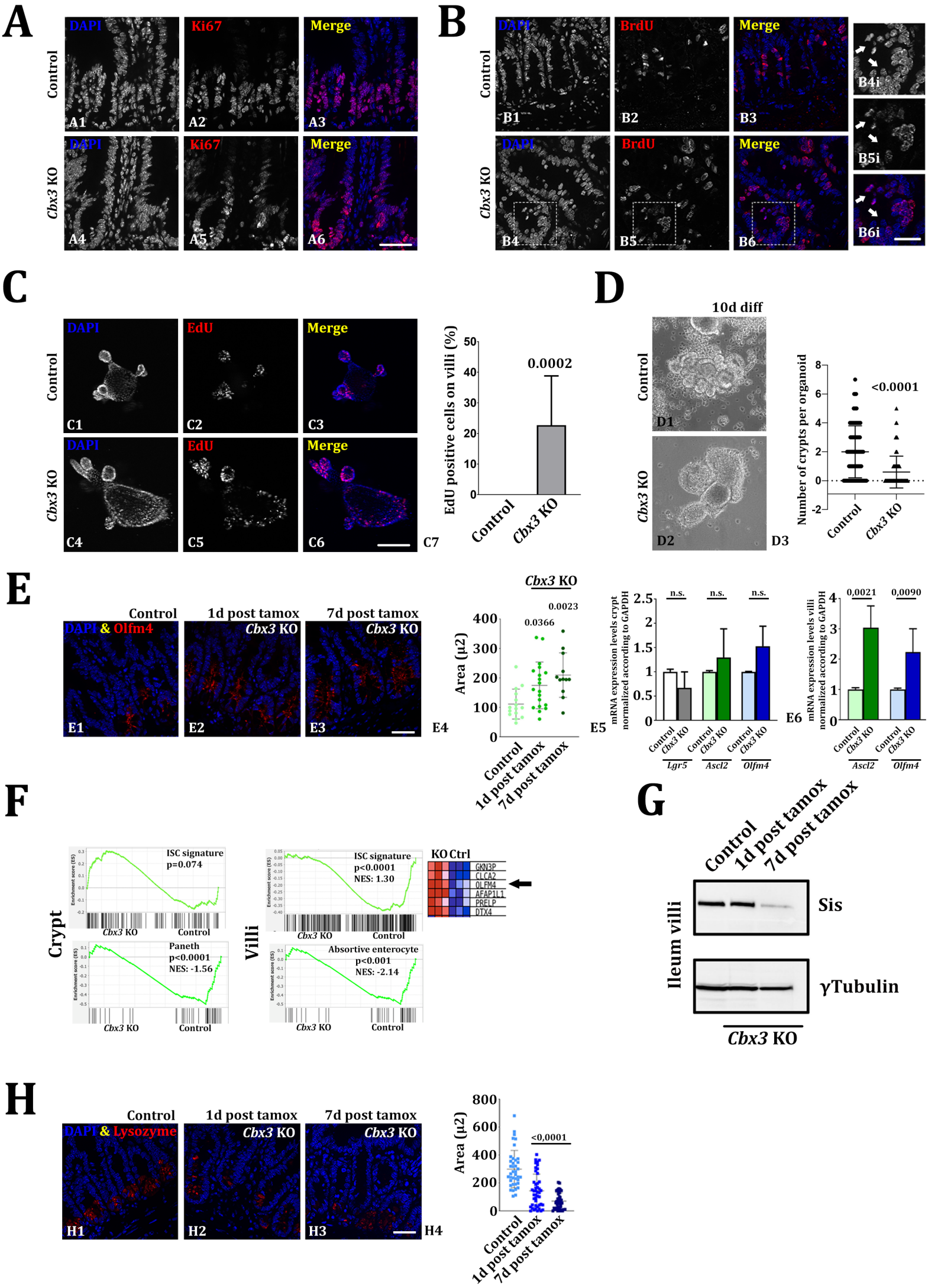
A
DAPI
Ki67
Merge
Control
Cbx3 KO
A1
A2
A3
A4
A5
A6
B
DAPI
BrdU
Merge
B1
B2
B3
B4
B5
B6
B4i
B5i
B6i
C
DAPI
EdU
Merge
C1
C2
C3
C4
C5
C6
C7
EdU positive cells on villi (%)
0.0002
Control
Cbx3 KO
D
10d diff
D1
D2
D3
Number of crypts per organoid
<0.0001
E
Control
1d post tamox
7d post tamox
DAPI & Olfm4
E1
E2
E3
E4
Area (µ2)
0.0366
0.0023
E5
mRNA expression levels crypt normalized according to GAPDH
n.s.
Lgr5
Ascl2
Olfm4
E6
mRNA expression levels villi normalized according to GAPDH
0,0021
0,0090
F
Crypt
ISC signature
p=0.074
Paneth
p<0.0001
NES: -1.56
Villi
ISC signature
p<0.0001
NES: 1.30
Absorbtive enterocyte
p<0.001
NES: -2.14
KO Ctrl
GKN3P
CLCA2
OLFM4
AFAP1L1
PRELP
DTX4
G
Control
1d post tamox
7d post tamox
Ileum villi
Sis
γTubulin
Cbx3 KO
H
DAPI & Lysozyme
H1
H2
H3
H4
<0,0001

Fig.3

A

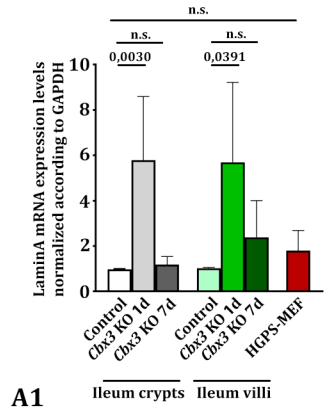

A1

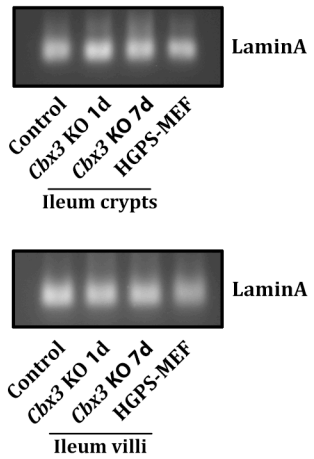

A2

B

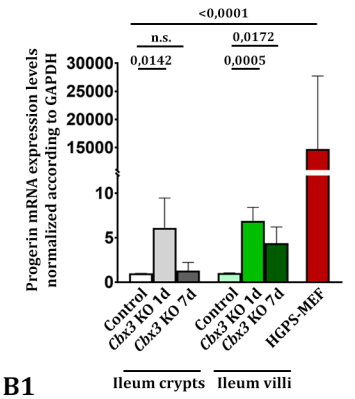

B1

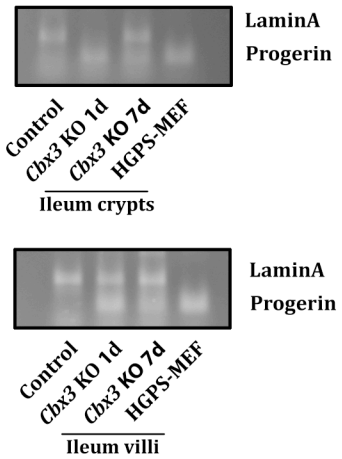

B2

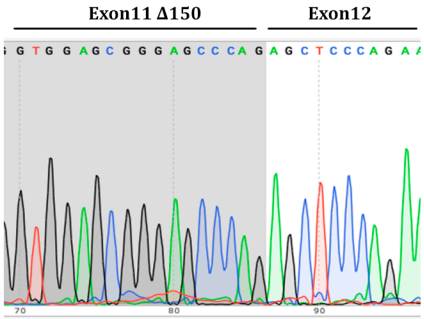

B3

C

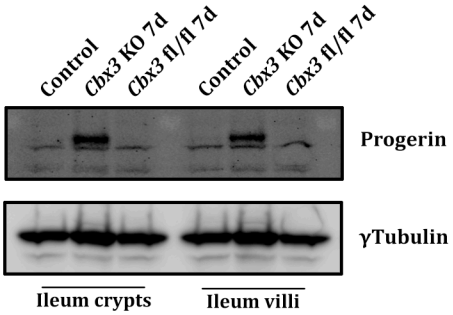

D

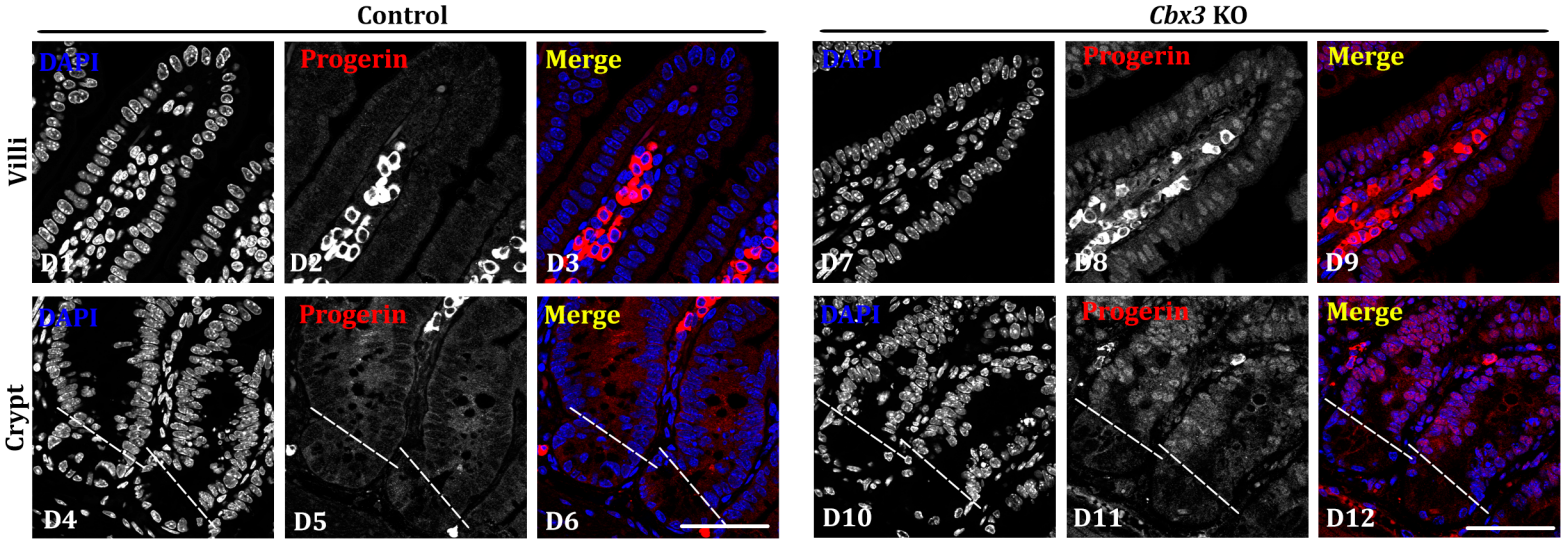

Fig.4

A

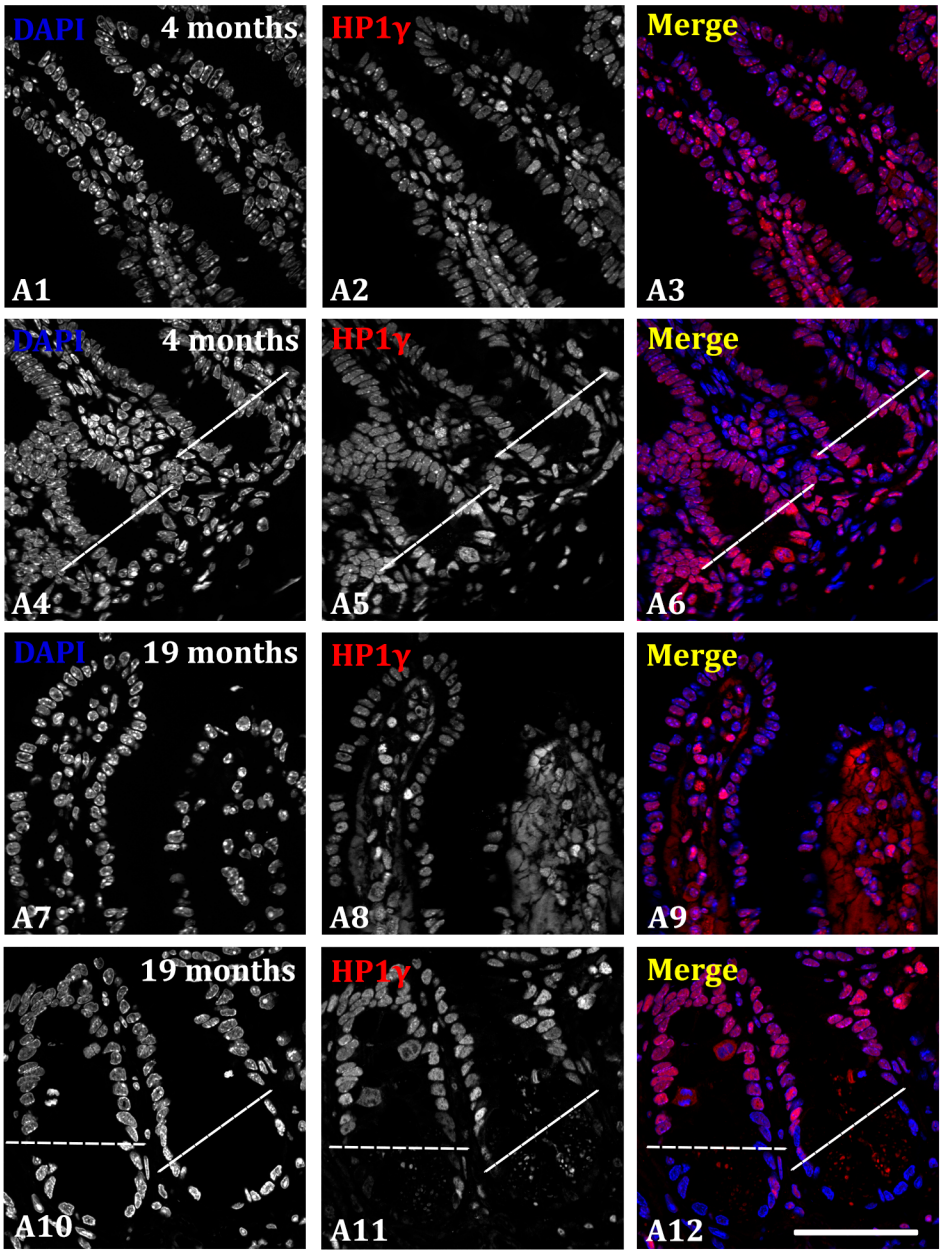
DAPI
4 months
HP1γ
Merge
A1
A2
A3
DAPI
4 months
HP1γ
Merge
A4
A5
A6
DAPI
19 months
HP1γ
Merge
A7
A8
A9
19 months
HP1γ
Merge
A10
A11
A12

B

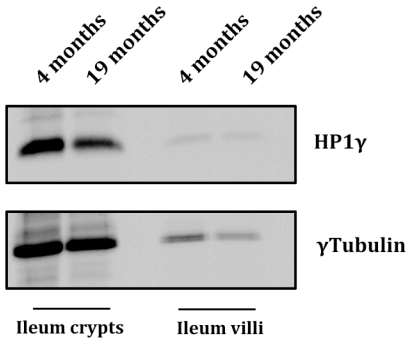
4 months
19 months
4 months
19 months
HP1γ
γTubulin
Ileum crypts
Ileum villi

C

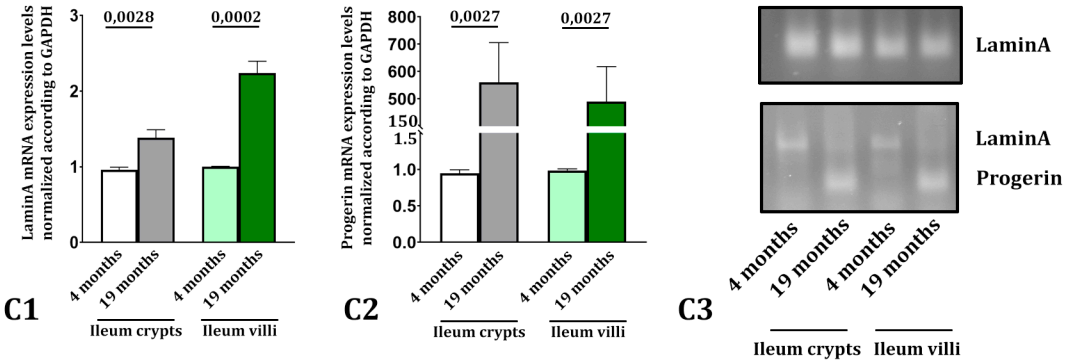
LaminA mRNA expression levels normalized according to GAPDH
0,0028
0,0002
4 months
19 months
4 months
19 months
Ileum crypts
Ileum villi
C1
Progerin mRNA expression levels normalized according to GAPDH
0,0027
0,0027
C2
LaminA
LaminA
Progerin
C3

D

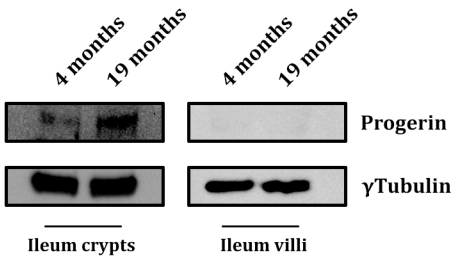
4 months
19 months
4 months
19 months
Progerin
γTubulin
Ileum crypts
Ileum villi

Sup. Fig.1

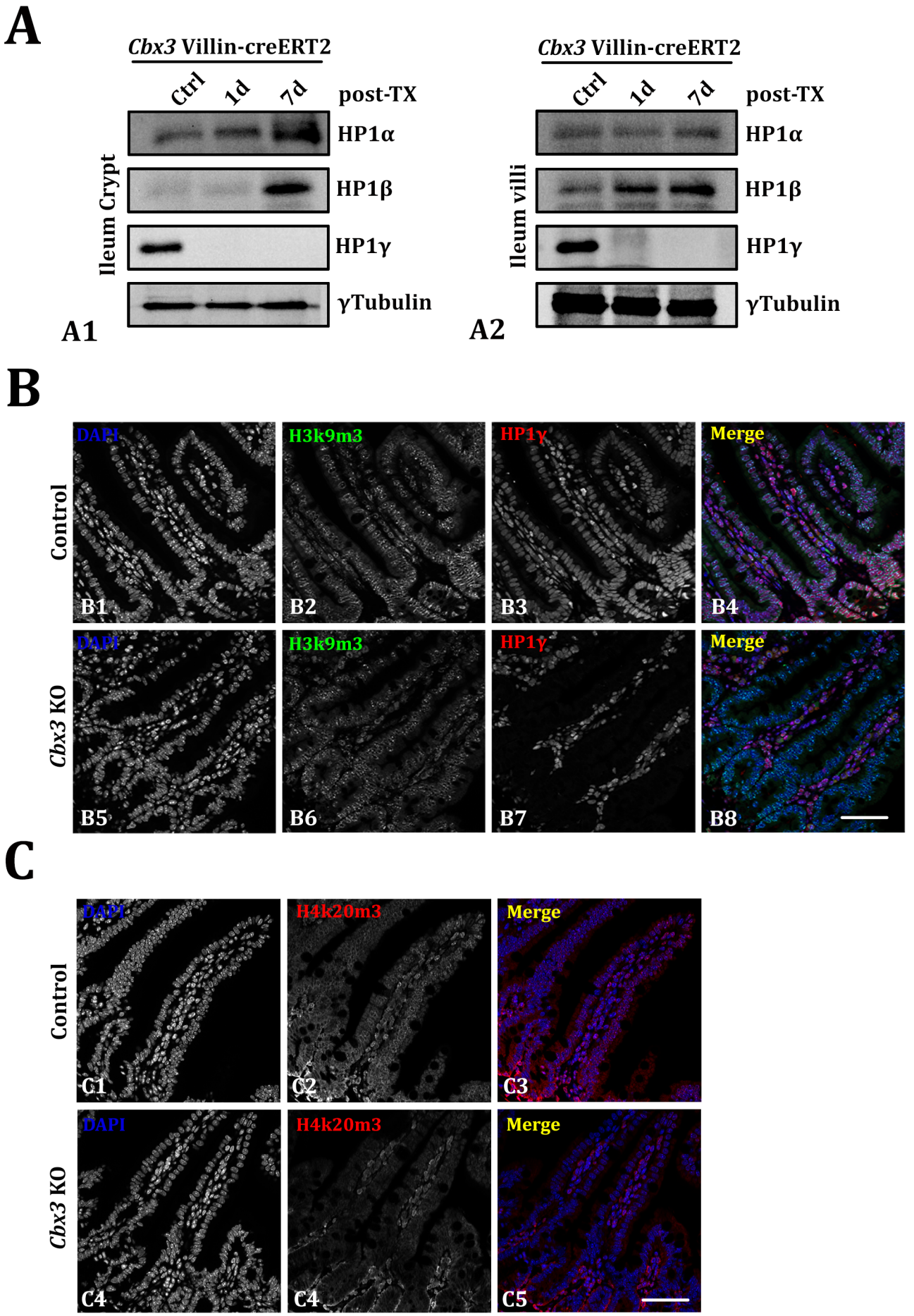
A
Cbx3 Villin-creERT2
Ctrl
1d
7d
post-TX
HP1α
HP1β
HP1γ
γTubulin
Ileum Crypt
A1
Cbx3 Villin-creERT2
Ctrl
1d
7d
post-TX
HP1α
HP1β
HP1γ
γTubulin
Ileum villi
A2
B
Control
Cbx3 KO
DAPI
H3k9m3
HP1γ
Merge
B1
B2
B3
B4
B5
B6
B7
B8
C
Control
Cbx3 KO
DAPI
H4k20m3
Merge
C1
C2
C3
C4
C4
C5

Sup. Fig. 2

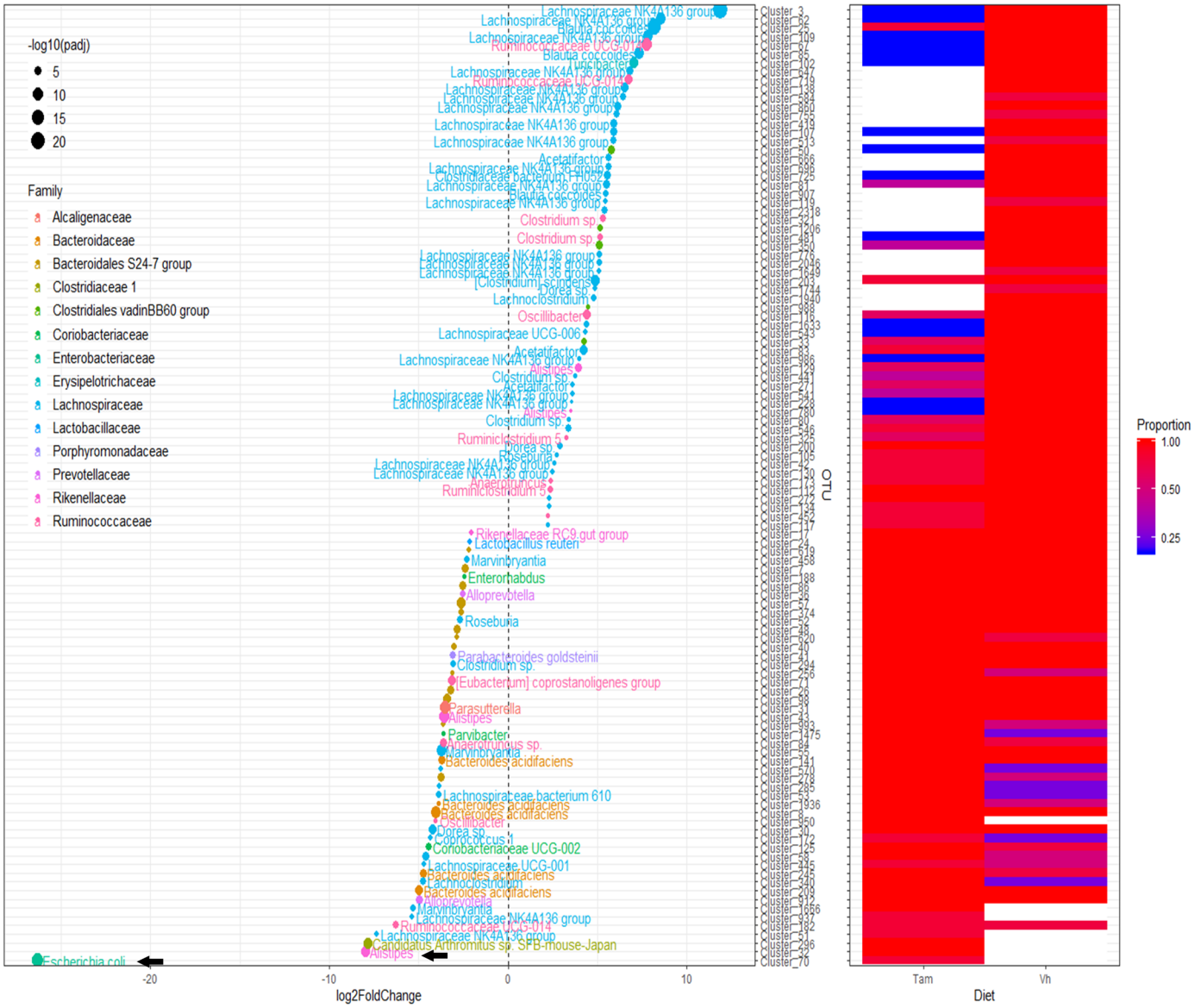

Legend: OTU (operational taxonomic units) significantly modified between young WT and KO CBX3 mice

Table1

Crypt	NumEvents.JC.only	SigEvents.JC.only
SE	35776	366 (226:140)
MXE	5874	173 (83:90)
A5SS	1563	55 (27:28)
A3SS	2629	70 (38:32)
RI	2304	164 (135:29)

Villi	NumEvents.JC.only	SigEvents.JC.only
SE	31118	374 (230:144)
MXE	5067	180 (89:91)
A5SS	1419	34 (19:15)
A3SS	2383	70 (33:37)
RI	2194	91 (61:30)